



Cite this: *Soft Matter*, 2022, 18, 5949

Long-range transport and directed assembly of charged colloids under aperiodic electrodiffusiophoresis†

Kun Wang,^a Samuel Leville,^a Behrouz Behdani ^a and Carlos A. Silvera Batista ^{*ab}

Faradaic reactions often lead to undesirable side effects during the application of electric fields. Therefore, experimental designs often avoid faradaic reactions by working at low voltages or at high frequencies, where the electrodes behave as ideally polarizable. In this work, we show how faradaic processes under ac fields can be used advantageously to effect long-range transport, focusing and assembly of charged colloids. Herein, we use confocal microscopy and ratiometric analysis to confirm that ac fields applied in media of low conductivity induce significant pH gradients below and above the electrode charging frequency of the system. At voltages above $1 V_{pp}$, and frequencies below 1.7 kHz, the pH profile becomes highly nonlinear. Charged particles respond to such conditions by migrating towards the point of highest pH, thereby focusing tens of microns away from both electrodes. Under the combination of oscillating electric fields and concentration gradients of electroactive species, particles experience aperiodic electrodiffusiophoresis (EDP). The theory of EDP, along with a mass transport model, describes the dynamics of particles. Furthermore, the high local concentration of particles near the focusing point leads to disorder–order transitions, whereby particles form crystals. The position and order within the levitating crystalline sheet can be readily tuned by adjusting the voltage and frequency. These results not only have significant implications for the fundamental understanding of ac colloidal electrokinetics, but also provide new possibilities for the manipulation and directed assembly of charged colloids.

Received 15th May 2022,
Accepted 13th July 2022

DOI: 10.1039/d2sm00631f

rsc.li/soft-matter-journal

1 Introduction

Electric fields are useful external inputs of energy because of the large parameter space available—amplitude, frequency, wave form—to tune colloidal transport and interactions. Upon application of an ac electric field, the charges inside and outside particles shift with time, leading to multipoles and induced flows.^{1–3} Electric fields induce a variety of surface and body forces that have facilitated applications such as pumping,⁴ separations,⁵ and electrodeposition.⁶ Recently, electric fields have been instrumental in advancing new paradigms in directed,^{7–9} dynamic,^{10,11} and reconfigurable assembly,¹² as well as in colloidal propulsion^{13,14} and directed transport.¹⁵

In directed assembly, external fields—usually of high frequency—are used to tune dipole-dipole interactions between

particles to bias the system towards more favorable and desired configurations.¹⁶ Field-directed assembly of anisotropic building blocks has produced structures with attractive photonic and phononic properties (*e.g.*, structural colors,¹⁷ anisotropic bandgaps¹⁸). On the other hand, tuning the temporal application of the fields, either through feedback control or toggling, produces colloidal crystals free of defects.^{9,19–23} In addition to dipolar interactions, fields at lower frequencies induce electrohydrodynamic and electroosmotic flows.^{4,24} In the vicinity of polarized electrodes, these flows mediate the assembly of particles into 2D structures. Moreover, if the symmetry of the particles is broken, such flows result in self-propulsion and dynamic assembly.^{13,25,26}

Faradaic reactions often lead to detrimental side effects, such as the formation of bubbles or the degradation of electrodes, when applying electric fields. Therefore, experimental designs often avoid faradaic reactions by using low voltages or high frequencies, so the electrodes behave as ideally polarizable.^{27,28} Low voltages guarantee working within the electrochemical window of the solvent, whereas high frequencies do not provide enough time for the charging of the double layer. In this context, high frequencies refer to values much higher than the electrode

^a Department of Chemical and Biomolecular Engineering, Vanderbilt University, Nashville, TN, USA. E-mail: silvera.batista@vanderbilt.edu;

Tel: +1 (615) 875-6195

^b Vanderbilt Institute for Nanoscale Science and Engineering, Vanderbilt University, Nashville, TN, USA

† Electronic supplementary information (ESI) available. See DOI: <https://doi.org/10.1039/d2sm00631f>

charging frequency (f_c). Typical values for f_c are in the order of hundreds of Hertz. However, studies have shown that even above f_c in water, faradaic reactions can still take place.^{29,30} This finding has important implications for the field of colloidal electrokinetics for two reasons. First, an increasing number of experiments use frequencies near 1 kHz, or combine steady and oscillating potentials, to control collective dynamics and propulsion.^{7,11,13,25,31} By balancing hydrodynamic and dipolar interactions, these experiments produce 2D colloidal materials with rich structural and dynamical behavior. Second, with some exceptions,^{32,33} effects associated with faradaic reactions, such as gradients of electrolytes near electrodes caused by the depletion/generation of electroactive species do not feature extensively in the mechanistic description of colloidal electrokinetics. Take as an example the intriguing theory of asymmetric rectified electric fields (AREF).^{34,35} This theory predicts that an oscillating electric potential can induce a steady electric field within the liquid when ions have unequal mobilities. The long-range steady electric field has been proposed as the mechanism inducing the levitation of charged particles near planar electrodes.³⁶ However, in its present form, the AREF theory assumes no flux for all ions at the electrodes; essentially, it does not account for faradaic reactions (electrochemistry), which will take place at frequencies below 1 kHz in water.

Recent experimental observations highlight the potential of coupling electric fields with induced gradients of electroactive species to control the assembly and transport of charged particles.^{31,37–39} In a recent work, we confirmed that electrodiffusiophoresis (EDP)—phoretic motion under diffusiophoresis and electrophoresis—was the mechanism responsible for the focusing and levitation of charged particles under uniform dc fields.⁴⁰ With the aid of confocal microscopy and ratiometric analysis, we observed that the passage of current through water induces significant pH gradients. Under those conditions, the diffusiophoretic contribution becomes large enough to balance and overcome the electrophoretic contribution. Moreover, the experimental results affirm the generality of EDP as an electrokinetic phenomenon that is not limited to a single solvent, as suggested by the initial experiments in DMSO.³⁸ Our goal in

this paper is to extend the experimental regime to low frequency ac fields. Andrei S. Dukhin and collaborators in the former Soviet Union established the framework for understanding EDP under ac fields (aperiodic EDP).^{41–43} In aperiodic EDP, time-dependent electric fields and gradients of electrolytes lead to directional motion of charged particles. It is important to highlight that, in contrast to dielectrophoresis,¹ a nonuniform electric field is not needed to achieve directional motion under aperiodic EDP; an important fact that was supported by the initial experimental results on the subject.^{43,44} In this work, we will show how faradaic processes under ac fields, and the motion of particles induced by EDP, can be used advantageously to effect long-range transport, focusing and assembly of charged colloids.

Herein, we use confocal laser scanning microscopy (CLSM) and ratiometric analysis to confirm that ac fields of low frequency (below 1.7 kHz), and applied in media of low conductivity, induce significant pH gradients that can persist above the electrode charging frequency for the system. Charged particles respond to the electrochemical conditions within the cell by migrating and focusing tens of microns away from the surface of the electrodes. By measuring the velocity of migration, we deduce the potential landscape experienced by the particles. These measurements demonstrate that significant wells in potential energy ($\sim 100k_B T$) can be induced with moderate electric fields. On the other hand, transport analysis provides further insights on the dynamics of charged particles. Afterwards, we turn our attention to the structural features of the aggregates in the focusing position. The large local concentration of particles near the focusing point leads to a disorder-order transition, whereby particles form crystals. We show that frequency and voltage readily tune the position and crystalline order within the levitating crystalline sheet.

2 Experimental methods and analysis

2.1 Model systems

The model systems used to study aperiodic EDP were carboxylate-functionalized fluorescent polystyrene particles (CB-PS) of 1.75 μm nominal diameter (Polyscience, 17686-5). All particles were dispersed in ultrapure deionized water ($18 \text{ M}\Omega \text{ cm}^{-1}$) with a concentration of approximately 0.05 w/v%. The zeta potential (ζ) of particles was measured *via* electrophoretic light scattering, using a Litesizer 500 (Anton Paar). The average ζ of the negatively charged CB-PS particles was $-65.4 \pm 3.1 \text{ mV}$.

2.2 Experimental set-up

Fig. 1 shows a drawing of the experimental setup. In a typical experiment, approximately 15 μL of suspension was confined in the device (electrochemical cell). The devices were built by separating two ITO-coated glass slides (Diamond Coatings, 8–10 Ohms) with a dielectric spacer, with nominal thickness of 120 μm (diameter 9 mm, Grace Biolabs, Cat. # 654002). The ITO slides were positioned so that the ITO coatings were in contact with the suspension. Prior to each experiment, the slides were cleaned by sequentially sonicating in acetone,

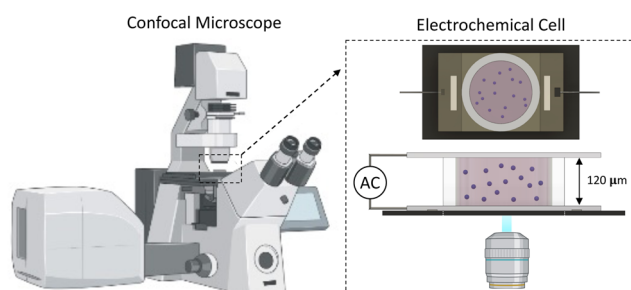


Fig. 1 Imaging the emission from SNARF-1 and fluorescent particles through confocal microscopy enables the simultaneous visualization of pH gradients and particle dynamics under ac fields. The device (electrochemical cell) consisted of two ITO slides separated by a dielectric spacer ($\approx 120 \mu\text{m}$ thick). Particles and SNARF-1 were excited at 405 nm and 514 nm, respectively.

isopropanol and DI water for 10 min in each solvent. Then, right before assembling the devices, the slides were treated with UV-ozone (UVO Cleaner Model 30, Jelight) for 10 min. The ac electric fields were applied using a function generator (Rigol DG1022). The frequency of the signal ranged from 1 Hz to 10 kHz, whereas the voltage varied from 0.1 to 5 V_{pp} (peak to peak).

The particles, the fluorescent dye, and the electrodes were simultaneously imaged using a Leica SP8 CLSM. Water (40×, 1.10 NA) and oil (100×, 1.47 NA) immersion objectives were used, while the pinhole was set to 1 Airy unit. The optical properties of particles were selected to avoid significant overlap with the ratiometric dye (SNARF-1). The particles were excited at 405 nm and their emission was collected at wavelengths between 420 and 470 nm. A high-speed resonant scanner (8 kHz) enabled high acquisition rates of up to 28 frames per second, at 512 × 512 pixel resolution. Two imaging modes were adopted. XZYT mode was used when a high time resolution was desired, whereas XYZT mode was used to capture the motion of all particles within a given imaging volume. The accumulation of particles at the focusing position scatter or block a substantial amount of the excitation light. Therefore, the intensity of excitation was adjusted during a scan, according to the position within the device, using Z-compensation. Adjustment of the laser intensity was particularly useful when imaging in the XYZT mode. Nonetheless, the ratiometric analysis enables the reliable quantification of pH, even when the excitation and emission intensity vary throughout the cell.

The center of the particles in the images was found by using the circle detection function (`imfindcircles`) in MATLAB. To quantify the crystallinity of an ensemble of particles, we calculated the six-fold bond orientational order parameter,

$$\Psi_{6,j} = \frac{1}{N_j} \sum_{k=1}^{N_j} e^{i6\theta_{jk}}.$$

For each spherical particle j , $\Psi_{6,j}$ is computed based on the number of nearest neighbors, N_j , where θ_{jk} is the angle between nearest neighbor spheres j and k , with an arbitrary reference direction. Using the center for each particle, we also calculate the Voronoi diagram for an image.

2.3 Measurements of pH during operation

Details on the procedure that was followed to measure pH in-operando can be found in our recent publication.⁴⁰ Briefly, pH was mapped using a ratiometric fluorescent dye, 5-(and-6)-carboxy SNARF-1 (ThermoFisher, C1270). The fluorescence emission of SNARF-1 changes from yellow-orange at acidic pHs to deep red at basic pHs.

The pH at any point can be extracted using the ratio of emission at two different wavelengths rather than using absolute intensity. In our experiments, SNARF-1 (100 μm) was excited at 514 nm, while dual emissions were detected at 580 nm and 640 nm. After acquisition of images, pH maps were calculated and plotted using an algorithm developed in Igor Pro, following the formula below:

$$\text{pH} = \text{p}K_a - \log\left(\frac{R_b - R}{R - R_a} \cdot \frac{I_{b,2}}{I_{a,2}}\right), \quad (1)$$

where R represents the ratio of intensities at two detection points, I_1 and I_2 , while R_b and R_a are the ratios of intensities at the basic (I_b) and acidic (I_a) end points. The average intensity at any given z -position was obtained using image analysis. It should be emphasized that using the ratio of signals at two different wavelengths minimizes the effect of fluctuations in focus, excitation intensities and concentration of the dye.

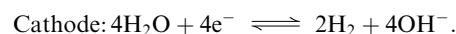
2.4 Analysis: transient pH under low frequency ac fields

A transport model provides insight on the pH profile within the electrochemical cell. We solve the Poisson–Nernst–Planck equations in the liquid domain for the OH[−], H⁺ and SNARF-1 species,

$$\frac{\partial n_i}{\partial t} + \nabla \cdot \mathbf{j}_i = R_i, \quad (2)$$

$$\mathbf{j}_i = -D_i \nabla n_i - n_i \mu_i \nabla \psi + n_i \mathbf{u}, \quad (3)$$

with the mobilities given by the Einstein–Smoluchowski equation, $\mu_{\pm} = D_{\pm} e z / k_B T$. D_i and n_i stand for the diffusivity and concentration of ionic species; \mathbf{u} and ψ are the velocity and electrical potential. The model solves the transient equation for conservation of ionic species.^{31,45,46} Diffusion, migration and convection determine the fluxes, \mathbf{j}_i , of ionic species. The reaction term, R_i , accounts for the equilibrium reaction of water ($2\text{H}_2\text{O} \rightleftharpoons \text{H}^+ + \text{OH}^-$) and dissociation of SNARF (SNARF^{−1} \rightleftharpoons SNARF^{−2} + H⁺) within the liquid domain. The dissociation equilibrium of the SNARF molecules occurs between species holding either one or two net negative charges.⁴⁷ The electroneutrality condition applies in the liquid domain since the size of the electrical double layer is of the order of tens of nanometers. Due to the oscillations in the field, we assume the average displacement due to electromigration is insignificant. Essentially, these assumptions simplify the physics to a diffusive mass transport problem. The oscillating voltage leads to an oscillating current at the electrodes. Therefore, the induced electrochemical reactions will be accounted using linearized Butler–Volmer kinetic expressions at the electrodes. Water electrolysis constitutes the most dominant faradaic reaction in the system, which produces protons at the anode and hydroxyl ions at the cathode, when carried out at neutral pHs:



At the bottom electrode, the other boundary condition is an oscillating potential (*versus* reference), $V = V_0 \sin(2\pi f t)$, while the top electrode remains grounded. In these calculations, the equilibrium potentials (E_{eq}) for the anodic and cathodic reactions are 0.80 and −0.41; these values were estimated using a Pourbaix diagram for water. The anodic transfer coefficients are the same for both reactions ($\alpha_a = 0.5$). For the reference exchange current densities, we use values equal to 3.98×10^{-3} and $1.38 \times 10^{-3} \text{ A m}^{-2}$. These values were measured using linear sweep voltammetry. We solved the coupled transport

equations using the finite element method as implemented in COMSOL Multiphysics, as well as the respective modules for the transport of dilute species and the tertiary current distribution. Further details on governing equations and parameters for the model are provided in the ESI.†

3 Results and discussion

We examined the response of charged particles to the electrochemical conditions induced by applying low frequency ac fields to aqueous suspensions. First, we report the results from measurements of pH within the experimental cell during operation. Then, we study the dynamics of particles in response to the changes of pH. Finally, we study the structure of particles once they are confined in the focusing position. In particular, we will focus on how the potential landscape experienced by charged particles can be used to effect disorder–order phase transitions in experiments with higher volume fractions.

3.1 Low frequency ac fields induce pH gradients

Fig. 2A and B show 3D confocal images of the volume within the electrochemical cell before and after applying an ac signal of 5 V_{pp} and 100 Hz, through an aqueous medium containing SNARF-1 and with conductivity (σ) of approximately 2 mS m⁻¹. The images show the view from the *x*-*z* plane of the volume between the electrodes (green slabs). The images combine the intensity collected at 580 nm (*I*₁, yellow-orange) and at 640 nm (*I*₂, red). Initially, the color throughout the cell is uniform, indicating a constant pH of \approx 7.1. However, after turning on

the field, the color within the cell becomes non-uniform, with the intensity from the red channel increasing substantially near the bottom electrode. The changes in relative intensity indicate that significant and measurable gradients in pH are taking place within the electrochemical cell.

Fig. 2C shows heat plots that condense the temporal and spatial distribution of pH during a single experiment, while Fig. 2D shows the pH profile for a single time (220 seconds). The values of pH reported in the heat plots were calculated using eqn (1) and the ratio of intensities from the two detection channels near 580 and 640 nm. The color scales in these plots range from bright red (pH 6) to purple (pH 7.6). The pH maps show that a profile forms within 10 s. Once established and until the field is turned off, the pH profile remains steady. From Fig. 2D, we can appreciate that the pH near the bottom electrode decreases to approximately 6.7. Moving further into the liquid medium, the pH rapidly increases until reaching a peak at 17 μ m. At this position, the pH is 7.4. Then, the pH begins to decay linearly to reach values as low as 6.4 near the top electrode. Therefore, the pH near both electrodes decreases below the initial values, prior to the application of the ac signal.

Fig. 3 shows the steady state profiles for fields generated by applying different voltages and frequencies. Although the pH profiles take similar times to reach steady state, their shape depends strongly on the parameters of the applied field. First, experiments performed at different voltages, but at the same frequency of 100 Hz, reveal that a threshold voltage is necessary to induce significant changes in concentration of H⁺. A clear pH gradient emerges when 1 V_{pp} is applied. Below that threshold, there is only a small linear gradient in pH. As the voltage increases, the peak in pH, occurring at tens of microns from the electrode surface becomes more conspicuous. On the other hand, experiments holding the voltage constant, while applying different frequencies, reveal that significant pH gradients persist at and above 1 kHz. Even at 10 kHz there is a small linear pH profile. Nonetheless, at higher frequencies, the peak in pH occurs closer to the bottom electrode. For example, at 1 kHz, the peak in pH occurs at approximately 7 μ m from the bottom

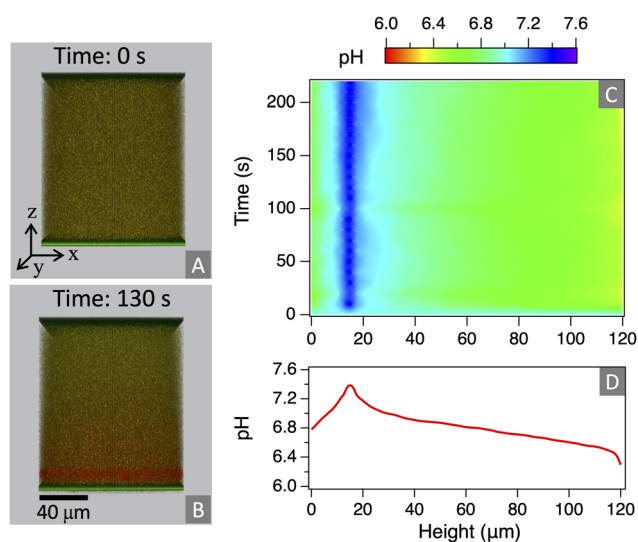


Fig. 2 Application of low frequency ac fields leads to noticeable changes of pH in aqueous electrolytes of low conductivity. (A and B) Confocal images of the volume between the electrodes (green slabs) before and after applying the field (5 V_{pp}, 100 Hz) for 130 seconds. Notice how application of the ac signal leads to changes in the emission of SNARF-1, indicating changes in pH. Panel C is a 2D heat map that condenses the pH for the entire experiment and at all positions. Panel D shows the pH profile at 220 s. After 10 s, the pH profile becomes highly nonlinear, and a peak emerges at approximately 17 μ m from the bottom electrode.

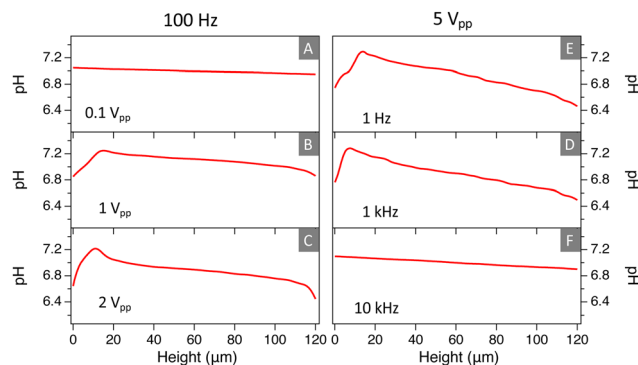


Fig. 3 A threshold in voltage is needed to induced highly nonlinear pH profiles. Panels (A–C) show profiles for different voltages (0.1, 1 and 2 V_{pp}) at the same frequency, 100 Hz. Panels (D–F) show profiles for different frequencies (10⁻³, 1 and 10 kHz) at the same voltage, 5 V_{pp}. Significant pH gradients persist at frequencies slightly 1 kHz.

electrode, in contrast to 17 μm at 100 Hz. In our previous work, we showed that pH profiles under dc fields resemble a sigmoidal curve.

3.2 pH gradients lead to long-range transport and focusing of charged particles

To study the behavior of charged particles under the oscillating potential, fluorescence intensities from particles and from the pH probe (SNARF-1) are recorded simultaneously. Fig. 4 shows images of particles and SNARF-1 before and 130 s after applying 5 V_{pp} at 100 Hz. Initially, the fluorescence intensities from particles and SNARF-1 are uniform throughout the cell. However, after the field is applied, particles near the top electrode begin to move downwards, while those near the bottom move upwards. After 100 s, most particles are focused at a position that is 17 μm from the bottom electrode. The accumulation of particles causes significant scattering and absorption of excitation light, resulting in noticeable changes in fluorescence of SNARF-1 above the focusing point. Nonetheless, ratiometric analysis accounts for those variations since it does not rely on absolute intensity to obtain local pH. The pH maps and pH profiles obtained from experiments with and without particles look similar (Fig. 3), suggesting that at the low volume fraction used in these experiments, the pH profile is not significantly affected by the presence of the particles. Consequently, the pH profiles are still determined by the electrochemical conditions of the system. Fig. 4G shows fluorescence intensity maps from particles, for all times in a single experiment. The intensity map shows that particles begin to focus as soon as the field is applied. Comparing the pH (Fig. 4F) and intensity profiles (Fig. 4H) after 220 s, it is apparent that particles focus at the point of maximum pH. This significant observation

suggests the peak in pH gradient induces a potential capable of focusing and trapping the particles.

Experiments with particles under different voltages and frequencies show that a nonlinear pH profile is needed to observe migration. Fig. 5 compares pH and intensity profiles for experiments at different frequencies and voltages. The changes in the shape of the pH profiles are mirrored in the intensity profiles from the particles. In contrast to 2 V_{pp} , focusing is not observed at 0.1 V_{pp} . Furthermore, in comparison to 100 Hz, the peak in pH for 1000 Hz occurs at approximately 8 μm . The intensity profile shows that the particles accumulate closer to the electrodes, but exactly at the same position where the peak in pH is taking place. To summarize, particles are transported to the point where the maximum pH values occur. Also, notice that although a nonlinear pH profile forms at 1 Hz, the rate of accumulation of particles is much smaller than at either 100 or 1000 Hz, confirming the important role that the pH profile plays.

Next, we look into the dynamics of the particles by measuring the migration velocity under different voltages, but at the same field frequency. To measure the velocity of the particles throughout the whole cell, two sets of experiments were performed. First, particles were allowed to completely sediment on the top electrode for at least 4 h. Then, once all particles were experiencing Brownian motion in the vicinity of the electrode, the device was mounted on the microscope stage. To measure the velocity below the focusing point, particles were allowed to sediment on the bottom electrode instead. Once the field was turned on, particles began to move in a band, whose position at any time was easily determined by tracking the intensity profile (Fig. S9 and S10, ESI \dagger). From such visual tracking, the velocity

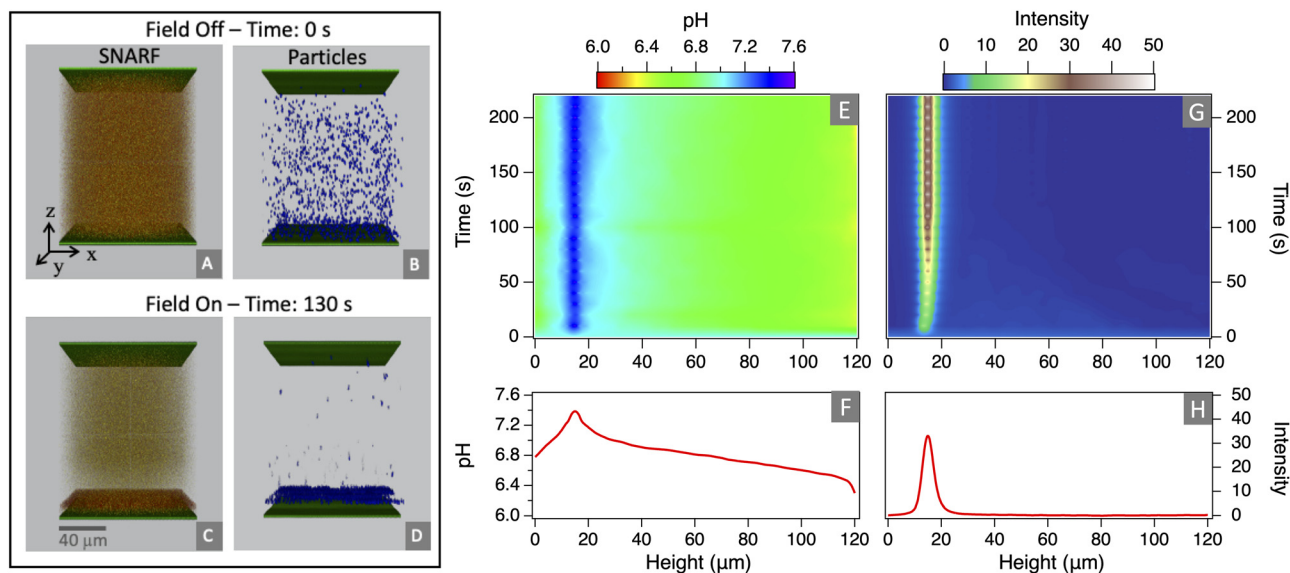


Fig. 4 Charged particles respond to applied ac fields by focusing at the position of maximum pH. (A–D) Confocal images of SNARF and fluorescent particles acquired simultaneously before and after applying an ac field (5 V_{pp} , 100 Hz) for 130 s. The images report volumes of cross section area equal to $106 \times 106 \mu\text{m}$, electrode gap of 120 μm , and detection from four channels centered at 435 nm (blue), 580 nm (yellow-orange), 488 nm (green) and 640 nm (red). Panels E and G are 2D heat maps that condense the pH and the fluorescence intensity from the particles for all times in a single experiment, while Panels F and H represent the pH and intensity profile for a single time, after reaching steady state. Notice how particles focus at the point of highest pH.

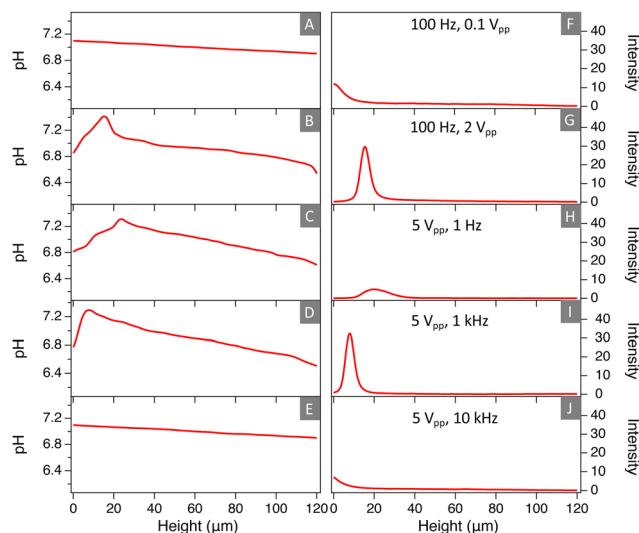


Fig. 5 Rapid migration and focusing of particles occur when highly non-linear pH profiles are induced. Profiles of pH (A–E) and fluorescence intensity of particles (F–J) for experiments at different voltages and frequencies. Linear pH profiles do not lead to significant motion; in those cases, particles move downwards due to gravity. For all the experiments, the respective heat maps condensing the pH profiles and intensity for all times are provided in Fig. S1–S4, ESI.†

was calculated by determining the position as a function of time.

Fig. 6 shows the velocity profiles of particles under different voltages. First, from top to bottom, particles initially accelerate until reaching a plateau about 20 microns from the electrode. The plateau in velocity extends for approximately 70 microns.

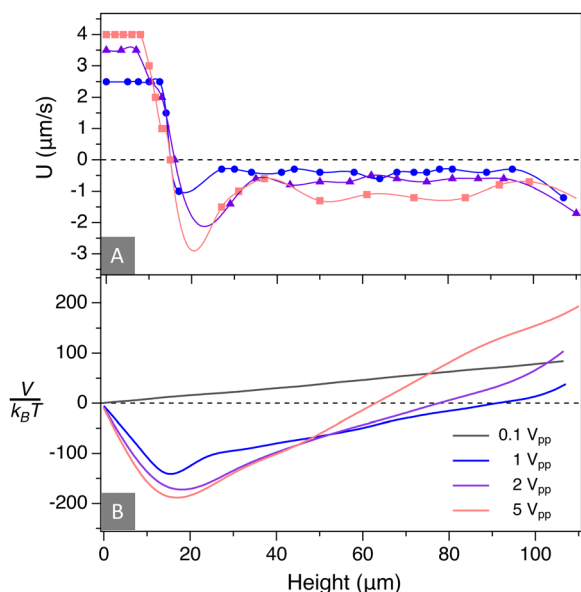


Fig. 6 (A) Velocity profile under different applied potentials and constant frequency, 100 Hz. The solid lines—provided for guidance—are interpolation of the data using cubic splines. (B) Potential landscape calculated from velocity profiles in Panel A. The potential energy (V) is given with reference to thermal energy ($k_B T$).

Then, 30 μm from the bottom electrode, particles briefly accelerate again, but rapidly decelerate towards the focusing point. For particles moving upwards from the bottom electrode, initially the velocity is constant for the first 15 μm , and then they quickly decelerate towards the point of zero velocity. The applied voltage influences the observed velocity. For example, at the plateau, the values of velocity are about $0.5 \mu\text{m s}^{-1}$ and $1 \mu\text{m s}^{-1}$ for $1 V_{pp}$ and $5 V_{pp}$, respectively. Similarly, close to the bottom electrode, the velocity of particles under $1 V_{pp}$ is about 60% the value under $5 V_{pp}$. Again, notice that although the particles reach the same final position, the dip in velocity before reaching the focusing point is quite sensitive to the applied voltage.

To get an idea of the relative importance of diffusive and convective transport, a Peclet number ($Pe = 2U_0R/D_0$) is calculated; U_0 and D_0 represent the free particle velocity and diffusivity. Using the values presented in Fig. 6, Pe can be as high as 25 for $5 V_{pp}$, and as low as 1 for $0.1 V_{pp}$, where no significant gradient is induced. Therefore, aperiodic EDP generates conditions where convective transport can dominate diffusive transport.

The previous section showed that points of zero velocity within the cell lead to focusing of particles far from the electrodes. In this regard, the devices work as electrokinetic traps. Therefore, the potential landscape provides further information about the capabilities of the system to focus and trap colloids in the z -direction. The potential landscape experienced by the particles, $V(z)$, can be deduced from the velocity profiles presented in Fig. 6 and the following formula,

$$V(z) = - \int_{z_0}^z F dz = -6\pi\mu R \int_{z_0}^z U(z) dz. \quad (4)$$

The force, F , is deduced from Stokes expression. Fig. 6B shows the potential experienced by the particles under ac fields generated by applying voltages of 0.1, 1, 2, 5 V_{pp} , at 100 Hz. First, the potential landscape for the particles under the lowest field, 0.1 V_{pp} , is similar to the gravitational potential. The curve shows a linear increase with height, as expected for particles experiencing a uniform gravitational force. The following expression gives the potential energy due to gravity,

$$V_g(z) = \frac{4}{3}\pi R^3 (\rho_p - \rho_f) gz, \quad (5)$$

where R represents the radius of particles; ρ_p and ρ_f are the density of particles and fluid, respectively. The particles move down at rates similar to sedimentation velocity ($\approx 0.1 \mu\text{m s}^{-1}$). Once the applied voltage increases, the potential landscape changes dramatically. For 1, 2, and 5 V_{pp} , the potential decreases rapidly until it reaches a minimum, approximately 17 μm from the bottom electrode. Then, the potential increases rapidly, albeit at a different rate. There are several noticeable features in these curves. First, the potential energy under EDP is substantial, and the particles experience potential wells that are higher than $100 k_B T$. Second, some properties of the potential landscape can be easily adjusted by changing the field parameters. The applied voltage adjust the depth as well as the stiffness of the potential well. Notice how the slope after the energy minimum changes with the applied voltage. All these

features provide potentially useful handles to manipulate the position and collective structure of charged colloids through directed assembly (see Section 3.4).

3.3 Mechanistic insights into the motion of particles under aperiodic EDP

The characteristic charging frequency of the electrodes is related to the finite time needed to form a double layer in an ac field, $\left(f_c = \frac{\sigma}{\epsilon} \cdot \frac{\lambda_D}{L}\right)$. σ , ϵ , and λ_D represent the conductivity, permittivity, and Debye length of the medium, whereas L stands for the characteristic length scale of the system. When the applied frequency is much lower than f_c , the double layer has enough time to form, and the faradaic reactions proceed at rates similar to those under direct current. In contrast, at frequencies much higher than f_c , the rate of faradaic reactions becomes negligible. The frequencies used in this study were both below and above the electrode charging frequency. For experiments without any indifferent electrolytes, as well as $\lambda_D = 30$ nm and $\sigma = 2$ mS m⁻¹, $f_c \approx 700$ Hz in our system. Thus, the electrolysis of water has enough time to occur. Consequently, the production of H⁺ and OH⁻ drives the formation of pH gradients. Moreover, substantial changes in pH have been reported even at frequencies as high as $10 \times f_c$.²⁹ These observations have important implications for the study of colloidal electrokinetics. Notice that this frequency range is often chosen for studying the propulsion and assembly of colloids.^{11,13,25,36} However, with some exceptions,^{33,48} the effect of faradaic processes, and the ensuing gradients of electroactive species, have not been an integral part of the physical description for the forces acting on charged particles under ac electric fields.^{7,31,36} An important barrier has been the need to measure concentration and fluxes of ionic species with high spatial and temporal resolution.

The transport model reproduces the basic features of the experiments. Fig. 7A shows pH profiles obtained from solutions of the PNP equations using an oscillating voltage, and electrode reactions, as boundary conditions. First, the model predicts a flat or small linear pH gradient at low voltages. As voltage increases, a peak in pH profiles emerges 5 μ m from the bottom electrode. Further away, the pH decreases monotonically. There are some differences with experimental pH profiles; for example, calculations predict larger peaks in pH that occur closer to bottom electrode. Despite those differences, the model confirms that an oscillating voltage, along with resultant production of H⁺ and OH⁻, leads to nonlinear and divergent pH profiles, like those shown in Fig. 3. In the model, the symmetry of the system is broken through the electrochemical boundary conditions. However, further research is needed to clarify the sources of asymmetry in the experiments. Also, it is important to note that these calculations were performed in the absence of SNARF-1 since equations eqn (8) is valid for monovalent ions. Nonetheless, when the SNARF ion are included, pH profiles resemble those shown in Fig. 7A.

As a first approximation,⁴³ EDP can be described by the addition of an electrophoretic and a diffusiphoretic term:

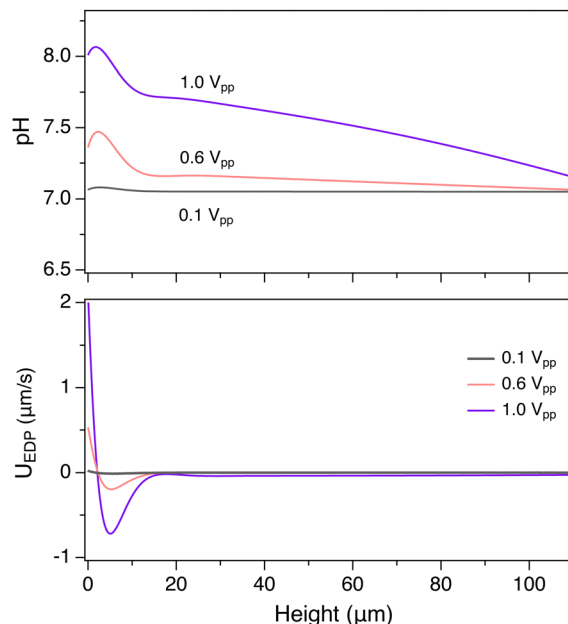


Fig. 7 (Top) pH profiles generated by solving the transport model at 100 Hz, and different oscillating voltages at the bottom electrode. The top electrode stayed grounded. (Bottom) Velocity profiles calculated using eqn (6)–(8) and the pH profiles shown in top panel.

$$U_{\text{EDP}} = U_{\text{EP}} + U_{\text{DP}} \quad (6)$$

For a thin double layer, U_{EP} is given by the Smolowchowski equation, but if the zeta potential does not change substantially during one period of the field, then U_{EP} approaches zero due to the oscillating nature of the signal. As a result, the upward and downward velocities needed to observe focusing must stem from the U_{DP} term. U_{DP} depends on the zeta potential, as well as the diffusivity and gradients of ionic species. Since more than two ions are present in the system, the theory developed by Squires and collaborators for multicomponent systems is suitable.⁴⁹ This theory provides an expression for U_{DP} that depends on the fluxes (j_i), the diffusivity of the ions (D_i) and the normalized zeta potential ($\tilde{\zeta}_p$):

$$U_{\text{DP}} = \frac{k_B T}{n_0^B} \left(M_+ \sum_+ \frac{j_i}{D_i} + M_- \sum_- \frac{j_i}{D_i} \right), \quad (7)$$

$$\text{with } -M_{\pm} = \frac{\epsilon}{e\eta} \frac{k_B T}{2e} \left[\mp \tilde{\zeta}_p + 4 \ln \left(\cosh \frac{\tilde{\zeta}_p}{4} \right) \right]; \quad (8)$$

n_0^B represents the bulk electrolyte concentration. To calculate U_{DP} , the fluxes for all species must be known. Values of the fluxes are readily obtained from calculations of pH profiles, as described above.

Fig. 7B shows the velocity profile calculated using the theory above. The curves reproduce several important features of the experiments. First, and most importantly, points of zero velocity appear where the corresponding maximum in pH occurs. Similarly, the velocity profiles show regions of positive velocity (close to the bottom electrode) and regions of negative velocity

(above the focusing point). Second, velocity profiles at 0.6 and $1 V_{pp}$ show a dip before reaching the point of zero velocity. Also, like in the experiments, focusing only happens at higher voltages. Lastly, the magnitude of the calculated velocity is similar to those observed in the experiments, $\sim 1 \mu\text{m s}^{-1}$, specially near the bottom electrode. Nonetheless, points of zero velocity in Fig. 7B occur closer to the electrode for 100 Hz. The overall agreement between modeling and experimental results supports the hypothesis that aperiodic EDP induces long-range transport and focusing of charged particles.

While developing the previous hypothesis that pH gradients and ac faradaic currents induce focusing, we also considered other alternatives. For example, if dielectrophoresis was the mechanism responsible for the directional motion of particles, a nonuniform electric field had to be present. However, the geometry of the device ensures that the potential is geometrically uniform. Another possibility is isoelectric focusing (IEF). In IEF, particles migrate under the influence of an electric field, and across a pH gradient, until they reach their point of zero charge. In our case, focusing would require that particles hold negative, as well as positive, charges on either side of the isoelectric point. However, our carboxylate-polystyrene particles show zero charge at low pH (~ 3) and do not acquire positive charges at any pH. Therefore, it will not be possible for particles to reach an isoelectric point where maximum pH occurs. A third potential mechanism is AREF; however, two important observations are not consistent with AREF.^{34–36} First, our experiments show that reactions are taking place, thus a key assumption in the AREF theory is violated. Second, particles only focus when there is a

divergent pH gradient. Without such pH profiles, particles neither levitate nor focus; such is the case when buffers or highly acidic solutions are used (see Fig. S5–S7, ESI†). Similarly, what controls the position of focusing is the point of highest pH, which can be modulated with frequency, voltage, initial pH and concentration of electrolytes.

3.4 Induced potential landscapes lead to disorder–order transitions

The ability of aperiodic EDP to focus and concentrate particles in a narrow region can be used to explore the phase diagram of the system. Therefore, we now look at the structures that form once particles have migrated from the bulk, which generally occurs after approximately 90 seconds (Fig. 3G). Fig. 8 shows images at the focusing position for different starting volume fractions. At low volume fractions, $\phi \approx 4.8 \times 10^{-4}$, hundreds of particles form clusters (Fig. 8A). Images at higher zoom (Fig. 8B and C) suggest little crystalline order and lack of close packing. As a quantitative measure of local crystallinity, the small value for the bond order parameter, $\Psi_6 \approx 0.04$, confirms the lack of local order. Furthermore, the lack of close-packing is reflected in the high interparticle distance— $d_{cc} = 1.7 \pm 0.1$, in particle diameters.

Setting the volume fraction to 2.4×10^{-2} leads to complete coverage for the cross-section at the focusing position, Fig. 8D. Images at higher magnification (Fig. 8E and F) reveal the outstanding transition into a highly organized array. Particles organize into hexagonally close-packed (hcp) crystal lattices, with a high bond order parameter, $\Psi_6 \approx 0.89 \pm 0.10$, and low

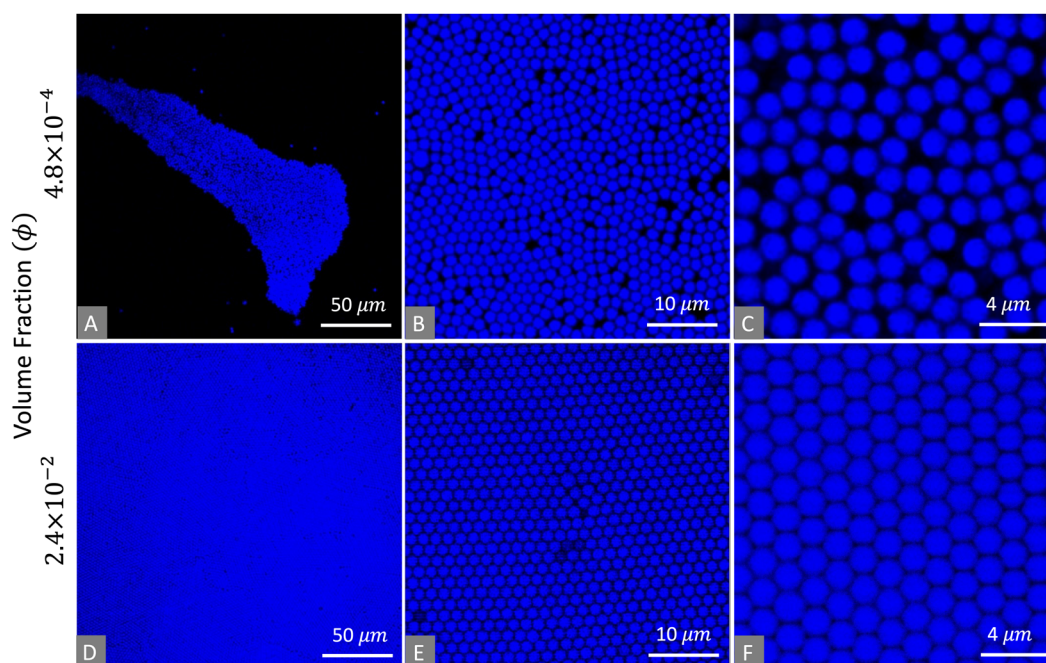


Fig. 8 Once at the focusing point, particles form aggregates of different local order. (A–C) Images at the focusing point for starting volume fraction of 4.8×10^{-4} . At low volume fractions, particles form aggregates with low local order. (D–F) Images at the focusing point for starting volume fraction of 2.4×10^{-2} . At higher volume fractions and surface coverage, particles form crystals with hcp lattices. In this experiment, an ac field ($5 V_{pp}$, 100 Hz) was applied and images were taken after all particles reached the focusing point. Colloidal crystals form 15–17 μm above the bottom electrode.

interparticle distance, 1.18 ± 0.03 . The crystal lattices include defects such as vacancies, grain boundaries and dislocations, as reflected by the standard deviation in Ψ_6 . Aperiodic EDP induces a phase transition by increasing the local concentration many folds.

The formation of clusters at low volume fractions suggests the presence of pair-wise hydrodynamic interactions. Nonetheless, we argue that the transition to hcp lattices originates from the equilibrium phase behavior of colloidal hard spheres. In this view, the potential landscape induced by aperiodic EDP transport, focus and concentrate particles to the point of a phase transition. Although detailed thermodynamic and kinetic analysis are beyond the scope of this work, it is instructive to assess the basic features of our observations in the context of field convective assembly. The change of volume fraction within a system can be described using a convection-diffusion equation that was originally formulated for sedimentation, and recently adapted for the case of electric fields.^{50–52} The convection-diffusion equation indicates that changes in volume fraction (ϕ) at a height (z), and time (t), occur through the contributions of convective and diffusive fluxes,

$$\frac{\partial \phi}{\partial t} + U_0 \frac{\phi K(\phi)}{\partial z} = D_0 \frac{\partial}{\partial z} \left(K(\phi) \frac{d}{d\phi} [\phi Z(\phi)] \frac{\partial \phi}{\partial z} \right). \quad (9)$$

U_0 represents the free particle velocity induced by the field; $K(\phi)$ accounts for the hindrance experienced by particles at higher concentrations, and $Z(\phi)$ stands for the compressibility factor of the suspension. In our case, aperiodic EDP causes the convective flux, with characteristic values of velocity presented in Fig. 6. The convective term could also stem from gravity,^{51,52} evaporation,^{53,54} dc fields,^{50,55} and dielectrophoresis.^{56,57}

Under equilibrium, the accumulation term becomes zero, while the convective and diffusive fluxes become equal. In other words, the Brownian force balances the external force due to Aperiodic EDP,

$$\frac{\partial \Pi(n)}{\partial z} = -\frac{\partial V(z)}{\partial z} \cdot n(z). \quad (10)$$

The Brownian force is written in terms of the osmotic pressure, Π , and the number density of particles, n . The external force and potential landscape induced by aperiodic EDP was shown in Fig. 6. The osmotic pressure is connected to the structures accessible to hard spheres *via* an equation of state,

$$Z(\phi) = \frac{\Pi(\phi)}{nk_B T}, \quad (11)$$

where the compressibility factor ($Z(\phi)$) captures the deviation from the osmotic pressure of an ideal solution, as the number density of particles increases. The specific form that $Z(\phi)$ takes depends on the phase of the system—liquid, solid, or glass.^{58,59} In these experiments, transport to the focusing position, and the subsequent accumulation of particles, increases the volume (area) fraction, thus inducing a transition from a fluid to a close-packed solid. For hard spheres, the coexistence of fluid and crystalline phases occurs at volume fractions between 0.49

and 0.54. For hard disks in 2D geometries, the coexistence region occurs for area fractions between 0.69 and 0.716.^{56,57}

We can tune the osmotic pressure, and therefore the structure formed by the particles, through the potential landscape (Eqn (10)). The tunability of the potential landscape (Fig. 6) with field parameters suggests a strategy to modulate the local order and position of the crystalline phases. First, the frequency of the field determines the position of minima in potential energy, thus providing a handle to control where crystallization occurs. Fig. 9A shows how crystallization can be induced at distances as far as 15–17 μm and as close to the electrode as 3 μm . Remarkably, when 5 V_{pp} is applied, the particles maintain their crystalline order at high frequencies, although the focusing distance changes. The highest focusing points occur at lower frequencies (1–100 Hz). As the frequency increases, the focusing point decays monotonically to zero. At frequencies above 1700 Hz, particles deposit on the surface of the electrode. As soon as particles are brought to the surface of the electrode, they disassemble, which correlates with the lack of divergent pH profiles at high frequencies.

On the other hand, the magnitude of the applied voltage changes the minimum in potential energy and the rate of change around it. Therefore, the applied voltage enables adjusting the order of the crystalline phases (see eqn (10)). Fig. 9B shows the bond order parameter and the interparticle distance for experiments under the same frequency, but different voltages. Ψ_6 is small for voltages below 2 V_{pp} , but it increases rapidly between 2 and 3 V_{pp} . The rate of change decreases above 3 V_{pp} until the highest values are achieved at 5 V_{pp} . The interparticle distance displays the opposite trend; d_{cc} decreases rapidly between 1 and 3 V_{pp} . Fig. 9C–F are representative images at each voltage. The images superimpose the contours identifying each particle and the respective Voronoi polygons. The images unequivocally demonstrate the effect of the voltage on the resultant structures. Crystalline phases with long-range order—as demonstrated by the presence of mostly hexagons in the Voronoi diagram—can be achieved at voltages above 3 V_{pp} (Fig. 9F). At lower voltages, the crystalline order deteriorates due to the inability of the field to keep particles tightly focused. For example, although the particles are all concentrated in a narrow band under 1 and 2 V_{pp} (Fig. S2, ESI†), many of them appear slightly out of focus, judging from their appearance as half-moons.

2D crystals of colloidal particles can be achieved using coplanar or parallel plate electrode geometries, by modulating dipolar interactions or EHD flows. However, what is unusual in our experiments is the combination of long-range transport, focusing, and crystallization far from the electrodes, through a single mechanism, in a simple geometry. Furthermore, crystallization away from the electrodes facilitate reconfigurability by minimizing irreversible adsorption. Fig. 9 shows that the bond order parameter can be adjusted with voltage, while maintaining focus away from the electrodes. It is important to highlight that particles transition from one state to another with significant speed (see video in ESI†). The change occurs in a couple of seconds, although achieving maximum order takes longer when cycling from low to high voltage, but still within

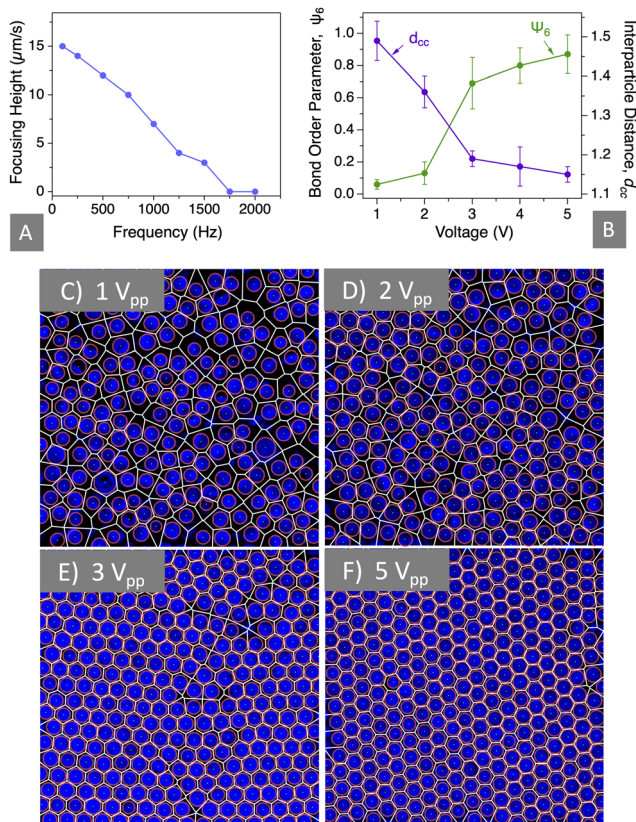


Fig. 9 Frequency of the field (Panel A) modulates the position of the colloidal crystals, whereas the applied voltage (Panel B) determines the local bond order parameter and interparticle distance. Voltages above 3 V_{pp} leads to highly ordered structures. (C–F) Representative images of the structures that form under different voltages. The images superimpose the Voronoi diagram and the fluorescent particles. Each particle is identified by its contour (red line) and center (white dots). The volume fraction of particles was 2.14×10^{-2} . Images represent areas equal to $30 \times 30 \mu\text{m}$.

10 seconds. In future work, the transition from one state to another could be optimized through toggled fields. Therefore, aperiodic EDP can be a tool for reconfigurable assembly.

Inducing EDP with ac fields is convenient. In dc fields, the progressive depletion of redox species leads to either increasing voltages (galvanostatic mode) or decreasing currents (potentiostatic mode). Both situations result in undesirable effects. In the first case, rising voltages often lead to degradation of electrodes; for ITO, degradation implies loss of transparency. In the second case, the driving force for assembly decreases with time. Also, relevant forces are induced in a simple geometry, using electrodes that do not need patterning through microfabrication. Nonetheless, it is important to keep in mind that low conductivities, and pH values close to neutral, were needed to observe focusing and crystallization.

4 Conclusions

In this article, we have employed aperiodic EDP to effect long-range transport, focusing and colloidal crystallization. Confocal microscopy and ratiometric analysis showed that applying low

frequency ac fields, ~ 1000 Hz, to aqueous media in a parallel plate geometry leads to significant pH gradients, with changes as large as 0.6 units. Transport analysis indicated that oscillating currents from the electrolysis of water can reproduce key features of the experimental pH profiles. The induced pH gradients cause the motion of charged particles over tens of microns towards a point of zero velocity, thus promoting focusing far from the electrodes. These results confirmed that uniform ac electric fields can be used to effect directional motion under aperiodic electrodiffusiophoresis. In contrast to dielectrophoresis, a geometrically nonuniform field is not required. Calculations showed that potential wells larger than $100k_B T$ tightly confine particles in the vertical direction. Furthermore, when experiments were performed at higher volume fractions, particles displayed a disorder–order transition into colloidal crystals with hexagonal lattices.

The insights presented in this article have implications for the manipulation of nanoparticles, directed assembly and fundamental aspects of colloidal electrokinetics. By inducing large potential wells under aperiodic EDP, the simple parallel-plate devices in this work essentially function as electrokinetic tweezers or traps.^{60,61} Therefore, the methods developed here could facilitate the trapping at the limit of a single nanoparticle, which can enable analysis at femtomolar concentrations. The potential landscapes under aperiodic EDP confine and concentrate particles in small regions. Therefore, aperiodic EDP facilitates directed and reconfigurable assembly. In particular, this setup can be used to explore the phase diagram of model systems that are available in limited quantities. We hope our findings catalyze further developments in ac colloidal electrokinetics, directed assembly and functional materials. Future work will focus on determining the impact of important parameters such as size, zeta potential and shape of the particles.

Conflicts of interest

There are no conflicts to declare.

Acknowledgements

The authors thank Vanderbilt University for resources provided through start-up funds. This work was partly supported by ACS PRF, under grant PRF# 61173-DNI5. Fig. 1 was created with BioRender.com.

Notes and references

- 1 T. Jones, *Electromechanics of Particles*, Cambridge University Press, Cambridge, UK, 2005.
- 2 V. Murtsovkin, *Colloid J.*, 1996, **58**, 341–349.
- 3 A. A. Harraq, B. D. Choudhury and B. Bharti, *Langmuir*, 2022, **38**, 3001–3016.
- 4 T. M. Squires and M. Z. Bazant, *J. Fluid Mech.*, 2006, **560**, 65–101.
- 5 T. Salafi, K. K. Zeming and Y. Zhang, *Lab Chip*, 2016, **17**, 11–33.

- 6 Y. Wang, L. Zhao, Y. Zhao, W. Y. Wang, Y. Liu, C. Gu, J. Li, G. Zhang, T. J. Huang and S. Yang, *Adv. Mater.*, 2018, **30**, 1870395.
- 7 J. R. Maestas, F. Ma, N. Wu and D. T. Wu, *ACS Nano*, 2021, **15**, 2399–2412.
- 8 J. J. Crassous, A. M. Mihut, E. Wernersson, P. Pfeleiderer, J. Vermant, P. Linse and P. Schurtenberger, *Nat. Commun.*, 2014, **5**, 5516.
- 9 J. Zhang, J. Yang, Y. Zhang and M. A. Bevan, *Sci. Adv.*, 2020, **6**, eabd6716.
- 10 J. Yan, M. Han, J. Zhang, C. Xu, E. Luijten and S. Granick, *Nat. Mater.*, 2016, **15**, 1095–1099.
- 11 Z. Wang, Z. Wang, J. Li, C. Tian and Y. Wang, *Nat. Commun.*, 2020, **11**, 2670.
- 12 A. A. Shah, B. Schultz, W. Zhang, S. C. Glotzer and M. J. Solomon, *Nat. Mater.*, 2015, **14**, 117–124.
- 13 F. Ma, S. Wang, D. T. Wu and N. Wu, *Proc. Natl. Acad. Sci. U. S. A.*, 2015, **112**, 6307–6312.
- 14 J. G. Lee, A. M. Brooks, W. A. Shelton, K. J. M. Bishop and B. Bharti, *Nat. Commun.*, 2019, **10**, 31–38.
- 15 Y. Wu, A. Fu and G. Yossifon, *Sci. Adv.*, 2020, **6**, eaay4412.
- 16 E. M. Furst, *Soft Matter*, 2013, **9**, 9039–9045.
- 17 A. A. Shah, M. Ganesan, J. Jocz and M. J. Solomon, *ACS Nano*, 2014, **8**, 8095–8103.
- 18 P. J. Beltramo, D. Schneider, G. Fytas and E. M. Furst, *Phys. Rev. Lett.*, 2014, **113**, 205503.
- 19 X. Tang, B. Rupp, Y. Yang, T. D. Edwards, M. A. Grover and M. A. Bevan, *ACS Nano*, 2016, **10**, 6791–6798.
- 20 T. D. Edwards, Y. Yang, D. J. Beltran-Villegas and M. A. Bevan, *Sci. Rep.*, 2014, **4**, 6132.
- 21 Z. M. Sherman and J. W. Swan, *ACS Nano*, 2016, **10**, 5260–5271.
- 22 Z. M. Sherman and J. W. Swan, *ACS Nano*, 2018, **13**, 764–771.
- 23 P.-K. Kao, B. J. VanSaders, M. D. Durkin, S. C. Glotzer and M. J. Solomon, *Soft Matter*, 2019, **15**, 7479–7489.
- 24 W. D. Ristenpart, I. A. Aksay and D. A. Saville, *J. Fluid Mech.*, 2007, **575**, 83–109.
- 25 F. Ma, X. Yang, H. Zhao and N. Wu, *Phys. Rev. Lett.*, 2015, **115**, 208302.
- 26 S. Gangwal, O. J. Cayre, M. Z. Bazant and O. D. Velev, *Phys. Rev. Lett.*, 2008, **100**, 058302.
- 27 C. L. Wirth, R. M. Rock, P. J. Sides and D. C. Prieve, *Langmuir*, 2011, **27**, 9781–9791.
- 28 C. L. Wirth, P. J. Sides and D. C. Prieve, *Phys. Rev. E: Stat., Nonlinear, Soft Matter Phys.*, 2013, **87**, 254.
- 29 R. An, K. Massa, D. O. Wipf and A. R. Minerick, *Biomicrofluidics*, 2014, **8**, 064126.
- 30 W. Y. Ng, Y. C. Lam and I. Rodríguez, *Biomicrofluidics*, 2009, **3**, 022405.
- 31 M. Rath, J. Weaver, M. Wang and T. Woehl, *Langmuir*, 2021, **37**, 9346–9355.
- 32 R. A. Rica and M. Z. Bazant, *Phys. Fluids*, 2010, **22**, 112109.
- 33 E. Yariv, *J. Chem. Phys.*, 2010, **133**, 121102.
- 34 S. M. H. H. Amrei, S. C. Bukosky, S. P. Rader, W. D. Ristenpart and G. H. Miller, *Phys. Rev. Lett.*, 2018, **121**, 185504.
- 35 S. M. H. H. Amrei, G. H. Miller, K. J. M. Bishop and W. D. Ristenpart, *Soft Matter*, 2020, **16**, 7052–7062.
- 36 S. C. Bukosky, S. M. H. H. Amrei, S. P. Rader, J. Mora, G. H. Miller and W. D. Ristenpart, *Langmuir*, 2019, **35**, 6971–6980.
- 37 N. Sidelman, M. Cohen, A. Kolbe, Z. Zalevsky, A. Herrman and S. Richter, *Sci. Rep.*, 2015, **5**, 13095.
- 38 C. A. Silvera Batista, H. Rezvantalab, R. G. Larson and M. J. Solomon, *Langmuir*, 2017, **33**, 10861–10867.
- 39 V. S. Doan and S. Shin, *Electrophoresis*, 2021, **42**, 2356–2364.
- 40 K. Wang, B. Behdani and C. A. Silvera Batista, *Langmuir*, 2022, **38**, 5663–5673.
- 41 E. S. Malkin and A. S. Dukhin, *Colloid J. USSR*, 1982, **42**, 396–401.
- 42 E. S. Malkin and A. S. Dukhin, *Colloid J. USSR*, 1982, **44**, 225–233.
- 43 Z. R. Ulberg and A. S. Dukhin, *Prog. Org. Coat.*, 1990, **18**, 1–41.
- 44 E. S. Malkin and A. S. Dukhin, *Kolloidn. Zh.*, 1982, **44**, 523–528.
- 45 K. Obata, R. V. D. Krol, M. Schwarze, R. Schomäcker and F. F. Abdi, *Energy Environ. Sci.*, 2020, **13**, 5104–5116.
- 46 Y. Wang, L. Zhao, Y. Zhao, W. Y. Wang, Y. Liu, C. Gu, J. Li, G. Zhang, T. J. Huang and S. Yang, *Adv. Mater.*, 2018, **30**, 1805686.
- 47 T. M. Żurawik, A. Pomorski, A. Belczyk-Ciesielska, G. Goch, K. Niedźwiedzka, R. Kucharczyk, A. Krężel and W. Bal, *PLoS One*, 2016, **11**, e0161353.
- 48 J. A. Fagan, P. J. Sides and D. C. Prieve, *Langmuir*, 2004, **20**, 4823–4834.
- 49 N. Shi, R. Nery-Azevedo, A. I. Abdel-Fattah and T. M. Squires, *Phys. Rev. Lett.*, 2016, **117**, 258001.
- 50 J. A. Ferrar and M. J. Solomon, *Soft Matter*, 2015, **11**, 3599–3611.
- 51 K. E. Davis, W. B. Russel and W. J. Glantschnig, *J. Chem. Soc., Faraday Trans.*, 1991, **87**, 411–424.
- 52 K. E. Davis and W. B. Russel, *Phys. Fluids A*, 1989, **1**, 82–100.
- 53 B. G. Prevo and O. D. Velev, *Langmuir*, 2004, **20**, 2099–2107.
- 54 J. D. Förster, J.-G. Park, M. Mittal, H. Noh, C. F. Schreck, C. S. O'Hern, H. Cao, E. M. Furst and E. R. Dufresne, *ACS Nano*, 2011, **5**, 6695–6700.
- 55 A. A. Shah, H. Kang, K. L. Kohlstedt, K. H. Ahn, S. C. Glotzer, C. W. Monroe and M. J. Solomon, *Small*, 2012, **8**, 1551–1562.
- 56 J. Zhang, Y. Zhang and M. A. Bevan, *J. Chem. Phys.*, 2020, **152**, 054905.
- 57 J. J. Juárez, S. E. Feicht and M. A. Bevan, *Soft Matter*, 2012, **8**, 94–103.
- 58 P. N. Pusey and W. v. Megen, *Nature*, 1986, **320**, 340–342.
- 59 P. N. Pusey, W. v. Megen, P. Bartlett, B. J. Ackerson, J. G. Rarity and S. M. Underwood, *Phys. Rev. Lett.*, 1989, **63**, 2753–2756.
- 60 C. Höller, G. Schnoering, H. Eghlidi, M. Suomalainen, U. F. Greber and D. Poulidakos, *Sci. Adv.*, 2021, **7**, eabd8758.
- 61 M. Krishnan, N. Mojarad, P. Kukura and V. Sandoghdar, *Nature*, 2010, **467**, 692–695.